

Cite this: *Phys. Chem. Chem. Phys.*, 2012, **14**, 9131–9136

www.rsc.org/pccp

PAPER

Porous gold nanodisks with multiple internal hot spots†

Jung-Sub Wi,*‡§ Satoshi Tominaka,‡ Kohei Uosaki and Tadaaki Nagao

Received 24th February 2012, Accepted 24th April 2012

DOI: 10.1039/c2cp40578d

For increasing the number of internal hot spots in the individual plasmonic nanoparticles, porous Au nanostructures were synthesized by a hybrid approach combining a physical process, which defined the overall shapes and dimensions of the nanostructures, and a chemical process, which incorporated nanopores inside the patterned nanostructures. This approach allows us to synthesize lithographically designed Au nanodisks containing numerous internal Raman hot spots in the form of nanopores. The increased number of hot spots successfully improved SERS intensity, and this experimental result was further elucidated by numerical electromagnetic simulations. The highly improved and homogeneous SERS intensities illustrate the great potential of the porous plasmonic nanodisks as a sensitive molecular imaging agent.

1. Introduction

The highly enhanced Raman signal obtained from the surface-enhanced Raman scattering (SERS) phenomenon has recently been widening its scope of application from molecular detection^{1–8} to molecular imaging,^{9–12} which is the visualization and characterization of biological processes at the cellular and molecular levels within intact living organisms.¹³ Besides the inherent character of Raman signals providing fingerprints by which the analyte molecules can be identified, the multiplexing capability,^{10,12} good photostability,¹⁴ and low background signal make the SERS-based molecular imaging technique a promising choice for various biomedical applications such as early cancer diagnosis. However, for practical uses by increasing the imaging depth, currently restricted to ~ 1 cm of tissues,^{11,12,15} one of the most essential prerequisites is to reliably generate numerous ‘Raman hot spots’ in a limited volume of plasmonic nanoparticles. In many cases, Raman hot spots, where a local electromagnetic field enhanced by surface plasmon resonance reaches its maximum value, generated from aggregates or assemblies of nanoparticles have been used, and these spots are located at the junctions of inter-particles.^{8–10,16,17} Therefore, the number of hot spots per single aggregate should be limited to only a few points. Recently, multiple hot spots from metal tip structures, such as Au nanostars, have been investigated, however only a part of those tips are activated by the incident light due to the distributions in the tip to tip length, their growth direction, and resonant frequency.^{18–21}

Here, we propose a simple and obvious way to increase the number of hot spots, which are generated at intra-particle. By incorporating chemically formed nanopores into physically fabricated plasmonic nanodisks, we succeeded in generating numerous Raman hot spots in a nanometer-scale volume of a plasmonic nanostructure and obtained a highly improved and uniform SERS intensity.

For the synthesis of porous Au or Ag nanostructures, there are several possible approaches; for example, (i) the precise control of nucleation and growth by electrodeposition, *etc.*, and/or the use of a foreign material substrate, which enables deposition of Au or Ag *via* the Volmer–Weber mechanism,^{22,23} and (ii) the use of smaller templates such as lyotropic liquid crystals or colloidal particles.^{24–27} The former may work well, though it requires a substrate possessing electrical conductivity for electrodeposition or a low binding energy to the deposits for the Volmer–Weber mechanism. The latter requires techniques for selectively depositing such templates with Au or Ag precursors within the nanospace. Owing to these restrictions, we focused on the chemical technique of dealloying, which has been used to form sponge-like nanoporous structures by the selective dissolution of more active element(s) from alloys.^{28–32} In contrast to the former approach mentioned above, initiation sites for the nanostructure formation are at the interface between the alloy phase and the dealloying solution; hence, dealloying is considered to be less dependent on the properties of the substrate.

In the present study, we demonstrated a unique physical–chemical combination method for synthesizing porous Au nanodisks as illustrated in Fig. 1. As the overall dimensions and internal nanostructures of the Au disks are, respectively, determined by the lithographic patterns and the dealloying conditions of co-sputtered AuCu alloy films, this approach is expected to enable us to obtain monodisperse SERS-active nanodisks containing high-density internal Raman hot spots in the form of nanopores.

International Center for Materials Nanoarchitectonics,
National Institute for Materials Science, 1-1 Namiki, Tsukuba,
Ibaraki 305-0044, Japan. E-mail: wi.jungsub@gmail.com

† Electronic supplementary information (ESI) available. See DOI: 10.1039/c2cp40578d

‡ Both authors contributed equally to this work.

§ Present address: Center for Nano-Bio Convergence, Korea Research Institute of Standards and Science, Daejeon 305-340, Korea.

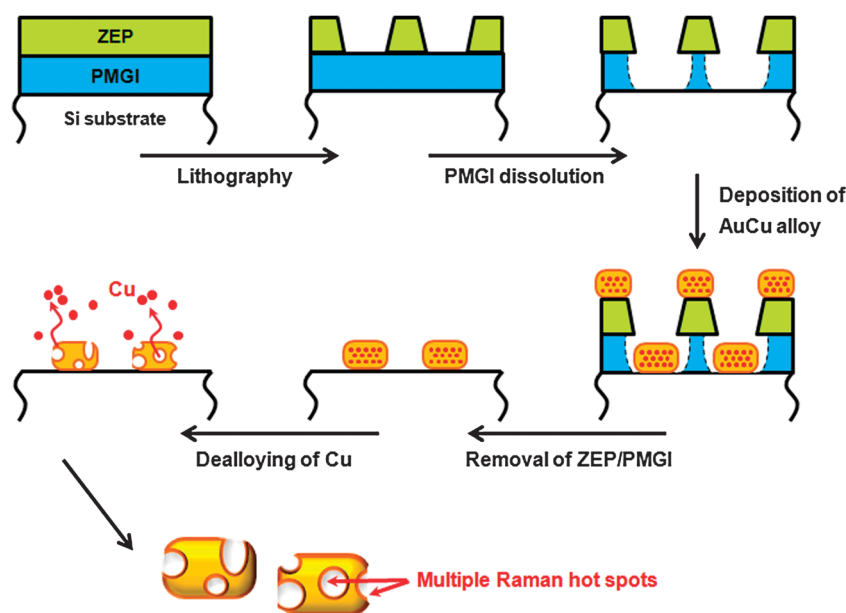


Fig. 1 Schematic illustration of the overall process in this study: electron beam (e-beam) lithography, wet chemical dissolution of PMGI, sputter deposition of the AuCu alloy, removal of ZEP and PMGI layers, and dealloying of Cu. ZEP and PMGI represent ZEP520A e-beam resist and polymethylglutarimide, respectively.

2. Experiments

Fig. 1 shows a schematic of the overall processing steps. To fabricate the lithographically patterned polymer template, 90 nm-thick polymethylglutarimide (PMGI, MicroChem) was spin coated onto a Si substrate and baked at 180 °C for 3 min. Then, a 20 nm-thick ZEP resist (ZEP520A, Nippon Zeon Co.) was spin coated onto PMGI and baked at 180 °C for 3 min. The electron beam exposures were conducted with a beam accelerating voltage of 50 keV. After developing the ZEP resist with a commercial developer (ZED-N50, Nippon Zeon Co.), the sample was immersed in an alkaline aqueous solution (NMD-3, JSR Micro) for 5 s to form an undercut profile in the PMGI resist. Then, AuCu alloy thin film was deposited by co-sputtering Au and Cu using a multi-target sputtering system (i-Miller CFS-4EP-LL from Shibaura; target substrate distance ~ 8 cm) at room temperature. As for the sputtering conditions, dc powers of 100 W and 200 W were applied, respectively, to Au (~ 22 nm min $^{-1}$) and Cu (~ 34 nm min $^{-1}$). Further details of sputtering conditions for various nanostructured Au used in this work are available in the ESI.† In order to selectively remove Cu, the samples were immersed in a concentrated aqueous solution of HNO₃ (Wako Pure Chemical Industries) for more than 90 min at room temperature. After preparing the porous nanostructures, 10 μ L droplet of Rhodamine 6G (R6G) methanol solution was spread on each 8 \times 8 mm² sample and then dried on a hot plate at 90 °C. Afterwards, SERS measurements were carried out using a confocal Raman microscope (alpha300S, WITec) with a laser having a wavelength of 532 nm. Although the power of the excitation laser was not measured for every sample, the Raman signal from the Si substrate was used as a reference and its intensity was always set to 50 CCD cts which corresponds to the incident laser of 1.4 mW in our experimental setup.³³ ‘CCD cts’ represents charge-coupled device counts. Because the R6G

molecule has its maximum molecular absorption at 530 nm,³⁴ the molecules are under the molecular resonance conditions with the incident light, and it is easy to obtain the Raman signal from the reference sample and compare it with the signal from the porous nanostructure. R6G-treated sample surfaces were mapped with a unit pixel mesh of 100 nm \times 100 nm and an accumulation time of 0.1 s pixel $^{-1}$. For plotting the SERS intensity, the background signal from the fluorescence of R6G was subtracted by the built-in software of the confocal Raman system. After masking the SERS peaks, the background level was fitted by the average intensity of neighboring frequencies.

3. Results and discussion

3.1. Characterization of the ultrathin nanoporous Au film

First, we synthesized and characterized nanoporous Au thin films in order to investigate the feasibility of the nanostructure formation from the sputtered AuCu alloys. Fig. 2a and b show the scanning electron micrograph (SEM) and the high-angle annular dark-field scanning transmission electron micrograph (HAADF-STEM), respectively, of an ultrathin porous Au film synthesized by co-sputtering a 80 nm-thick AuCu alloy film followed by selective dissolution (or dealloying) of Cu. These images clearly show that the dealloying of the co-sputtered AuCu alloy succeeded in the formation of nanopores without post-annealing of the deposit, thereby indicating its compatibility with lithographic patterns.

Before discussing the SERS measurements, the samples were characterized further as follows. The X-ray diffraction (XRD) patterns (Fig. 2c and Fig. S1 in the ESI†) clarified that the as-deposited film consisted of an alloy phase of Au₅₀Cu₅₀, which was determined from the (111) Bragg peak located at 40.59° by following Vegard's Law on the basis of the assumption of a solid solution and a small amount of polycrystalline Cu phases.

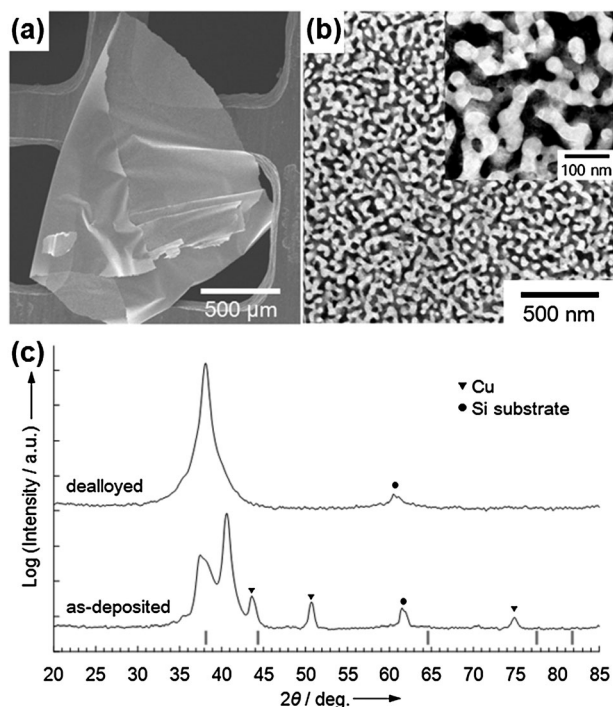


Fig. 2 Characterization of the quasi two-dimensional, ultrathin nanoporous Au film synthesized by co-sputtering and dealloying: (a) SEM image, (b) HAADF-STEM images, and (c) thin film XRD pattern collected on an imaging plate at a fixed incident angle of 20° (Cu K_α). The bottom lines in (c) show the Bragg peak positions of pure Au.

This alloy film became a quasi two-dimensional pure Au nanostructure after dealloying. Judging from the absence of other Bragg peaks originating from the alloy phase, the XRD pattern was found to exhibit a strong (111) orientation for the alloy phase, which was interestingly maintained even after dealloying. Regarding the composition, the energy-dispersive X-ray spectroscopy during the TEM observation clarified the presence of a tiny amount of remaining Cu in the Au ligament ($\text{Au}_{94}\text{Cu}_6$). X-ray photoelectron spectra (XPS) shown in the ESI† (Fig. S2) indicated that residual Cu existed as CuO, as inferred from the presence of shake-up satellites between the two peaks of Cu 2p.^{35,36} The angle-resolved XPS analysis indicated that CuO existed as an impurity remaining on the surface of Au ligaments because the Cu content increased from 3 at% at a takeoff angle of 68° to 5 at% at 12° . Although it is expected that these small amounts of Cu impurities, which are also known as one of the plasmonic materials,³⁷ would not be critical to the SERS activity, further improvement of the dealloying process is required to minimize impurities on the Au surface and to maximize the number of adsorbed molecules on the surface.

3.2. Impact of multiple nanopores in Au nanodisks on SERS intensities

When the AuCu alloys were applied to the lithographically patterned polymer templates, namely nanopores, this chemical dealloying enabled us to obtain Au disks with nanopores, as shown in Fig. 3. As the lateral size and the thickness of nanodisks are determined by the conditions of lithography and sputter deposition, respectively, there is no noticeable variation of

overall dimensions in several batches. Many thorough studies have revealed that the ligament size and porosity of the dealloyed structures are controllable by tuning conditions such as the alloy composition and dissolution rate,^{36,38,39} and here Au nanodisks with three different internal structures were synthesized by applying different sputtering conditions (Fig. 3b–d and ESI†). Because this nanostructure formation does not need any capping agents such as surfactant molecules, which are generally used in the colloidal synthesis of Au nanoparticles, the pure plasmonic structure with the nanoscale granular morphology observed in Fig. 3d is of quite interest.

The SERS characteristics of the Au disks were analyzed using a scanning confocal microscope after treating the disks with R6G at a concentration ranging from 1 nM to 1 mM. For the purpose of comparison, a solid Au disk with a diameter of 220 nm and a height of 60 nm was also prepared by the evaporation of pure Au (Fig. 3a) and used as a control sample. As compared to nanospheres typically used as a SERS substrate, the solid Au disk induces more intense surface plasmon field due to its large aspect ratio of diameter and thickness (Fig. S3 in the ESI†). The overall dimensions of the Au disks shown in Fig. 3a–d were maintained the same in order to investigate the relation between the morphology of the Au film and the SERS enhancement. The SERS map shown in Fig. 3g, which was obtained from the 0.1 mM R6G-treated Au nanodisk array shown in Fig. 3e, visualizes the spatial distribution of the integrated Raman intensity associated with an in-plane bending of a xanthene ring in the R6G molecules from 590 to 640 cm^{-1} .^{40,41} By comparing the SERS map (Fig. 3g) with the SEM image (Fig. 3e), it is clear that the Raman signal is enhanced by the Au disks. In addition, the overall appearances of the SERS maps in Fig. 3f–h show a growing tendency of the SERS signal with increasing porosities.

Representative SERS spectra of the 0.1 mM R6G-treated Au nanodisks with different porosities are plotted in Fig. 3i for a more direct comparison. The peak positions in the SERS spectra were accurately assigned to the vibrational bands of the R6G molecules reported in the reference articles.^{40,41} In order to discuss the nanostructure effects, the spectra were normalized using intensities of the leftmost peak located at 520 cm^{-1} , which originated from the Si substrate. It is absolutely clear that the SERS intensities from R6G molecules increased with the porosity of the Au disk.

The changes in SERS intensity with the film porosity for a broad range of R6G concentrations are summarized in Fig. 3j. The increase and saturation of the Raman signal at the R6G concentration were consistent with other reports,^{42,43} and the increase of the SERS intensity with the film porosity was consistently confirmed for the R6G concentrations ranging from $1\text{ }\mu\text{M}$ to 1 mM. As indicated by the circular and triangular dots in Fig. 3j, the maximum SERS intensity at the saturation level increased by about five times by changing the internal structure of the Au disk from the solid to the nanoporous film. Also, it could be confirmed that the minimum detection level was improved by three orders of magnitude from $1\text{ }\mu\text{M}$ to 1 nM.

3.3. Three-dimensional electromagnetic simulation

In order to theoretically elucidate the impact of the nanostructures on SERS enhancement mentioned above, the local

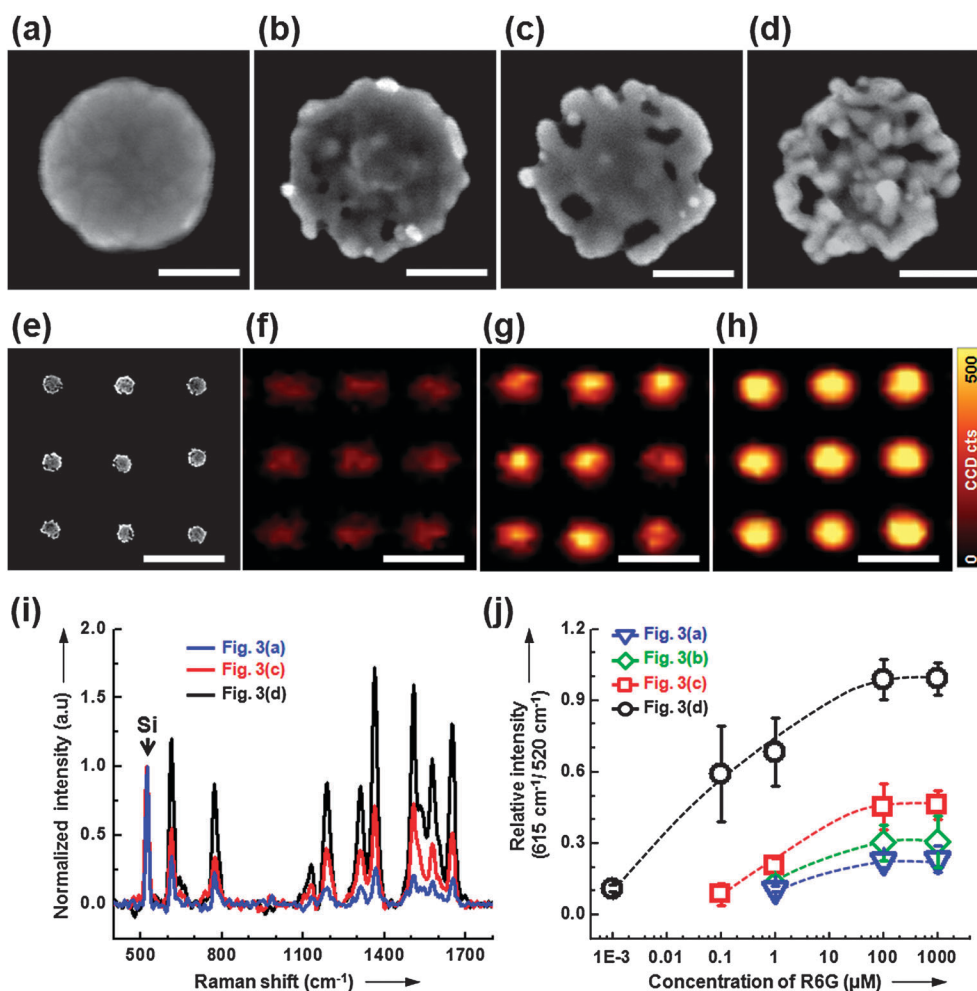


Fig. 3 (a–d) SEM images of lithographically patterned Au disks with controlled porosities. (e) Low-magnification SEM image of (c). (f–h) Two-dimensional intensity maps of the SERS signal integrated from 590 to 640 cm^{-1} from the Au disk arrays: (f) from Fig. 3a, (g) from Fig. 3c, and (h) from Fig. 3d. For the SERS measurement, the sample was treated with 0.1 mM Rhodamine 6G methanol solution. The scale bars in (a–d) and (e–h) are 100 nm and 1 μm , respectively. (i) Representative SERS spectra (Baseline signals were corrected.) and (j) averaged SERS intensities of the peak of 615 cm^{-1} from the R6G-treated Au nanodisks with different porosities: non-porous (blue, Fig. 3a), less porous (green, Fig. 3b), porous (red, Fig. 3c) and highly porous (black, Fig. 3d). The intensities were normalized using the Si signal located at 520 cm^{-1} . Dashed lines are visual guides. For plotting this graph, nine SERS spectra from nine different Au disks in each SERS map were measured, and the values were averaged.

electric field contours of the Au disks on the Si substrate were calculated using three-dimensional finite-difference time-domain simulation program (Lumerical FDTD Solution 6.5), as shown in Fig. 4. The simulation mesh was set to a 1.0 nm cubic grid, and perfectly matched layers were used as a boundary condition. The isolated Au nanodisks were placed on the infinite Si substrate and illuminated from the top by a linearly polarized plane wave with a wavelength of 530 nm. As electromagnetic field enhancement from a localized surface plasmon resonance is known to be the major mechanism for SERS, contour maps visualizing enhanced electric fields of $|E/E_0|^2$, where E_0 and E are the amplitudes of the incident and enhanced electric fields, respectively, are shown in Fig. 4a–c. The calculated field contours in Fig. 4a and b were based on the SEM images in Fig. 3d and respectively. The red-colored spots in the field contours of the porous Au disks (Fig. 4a and b) clearly show that the local electric field amplitudes near the nanoscale gap or protrusions are significantly higher than that at the plain Au disk (Fig. 4c). This qualitatively corresponds to the

experimental results well, although the two-dimensional SEM images were simply elongated along the z -direction to be 60 nm-high Au disks, whose smooth sidewalls were assumed to limit excessive simulation parameters.

For the quantitative comparison between the simulated and experimental results, the pixel-weighted sum of $|E/E_0|^4$ values, which are proportional to the maximum intensity of the SERS signal,^{44,45} was calculated for the entire area of each field contour in Fig. 4a–c. As shown in Fig. 4d, the sum value of the highly porous Au disk (Fig. 4a) was eight times higher than that of the plain Au disk (Fig. 4c) and it was consistent for several different porous Au disks (Fig. S4 in the ESI†). These simulation results are reasonably matched with the five-fold improvement observed from the experimental results (Fig. 3j). In addition, the increased number and areal fraction of the red-colored spots associated with the pore formation made it possible to increase the chances of the R6G molecules meeting the Raman hot spots. Therefore, this contributed to the improvement of the molecular detection sensitivity as well as

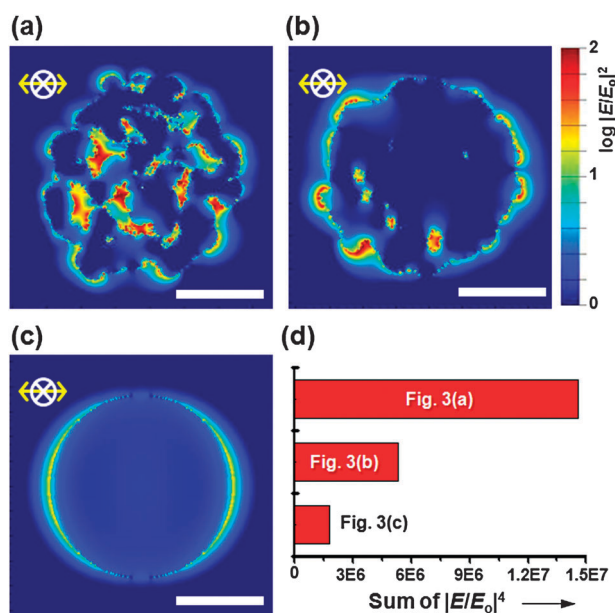


Fig. 4 Three-dimensional FDTD simulation for elucidating the Au nanostructure effect. (a–c) Squared magnitudes of the local electric field amplitudes. Incident light having a wavelength of 530 nm enters in the z -direction and is polarized in the x -direction, as indicated by the white and yellow arrows, respectively. All the scale bars are 100 nm. (g) The pixel-weighted sum of the $|E/E_0|^4$ values calculated from the entire area of the field contours in (a–c).

the increase of the brightness of the SERS signal from a single nanoparticle, which should be useful to increase the information depth of *in vivo* or *in vitro* molecular imaging. More detailed analysis of the simulated field enhancement and its statistics are described in the ESI† (Fig. S4). It is also noteworthy that the irregular shapes and dimensions of the internal nanostructure enabled activation of the hot spots in the Au disk for a broadband spectrum of incident light, as compared to the solid Au disk (Fig. S5 in the ESI†).

4. Conclusion

Here, we have presented a hybrid approach that combines a physical process, which defines the overall shapes and dimensions of plasmonic nanostructures, with a chemical process, which enables the incorporation of nanopores inside the physically patterned nanostructure. This approach allowed us to synthesize the lithographically designed plasmonic nanostructures with numerous internal hot spots in the form of nanopores, and concomitantly to enhance SERS activities, which were confirmed by experimental comparison with Au nanostructures of different porosities and their simulated local electric field amplitudes. Although the current plasmonic nanostructures are attached on a Si substrate, release of nanostructures from such substrates is simply possible by including a dissolvable sacrificial polymer layer underneath the nanostructures, and also the massive synthesis can be realized with the low-cost, high-throughput nanoimprinting process, as demonstrated in the previous reports.^{33,46,47} Therefore, considering the present results, we conclude that porous Au nanodisks on the substrate are applicable as a highly sensitive molecular detection platform,

and expect that such nanodisks released from the substrate can be useful as molecular imaging reagents.

Acknowledgements

This work was supported in part by KAKENHI (Grant No. 20671002) from Japan Society for the Promotion of Science and by the World Premier International Research Center Initiative on “Materials Nanoarchitectonics” from MEXT (Japan).

References

- 1 J. N. Anker, W. P. Hall, O. Lyandres, N. C. Shah, J. Zhao and R. P. Van Duyne, *Nat. Mater.*, 2008, **7**, 442–453.
- 2 X. X. Han, G. G. Huang, B. Zhao and Y. Ozaki, *Anal. Chem.*, 2009, **81**, 3329–3333.
- 3 S. Chen, M. Svedendahl, M. Kall, L. Gunnarsson and A. Dmitriev, *Nanotechnology*, 2009, **20**, 434015.
- 4 J. F. Li, Y. F. Huang, Y. Ding, Z. L. Yang, S. B. Li, X. S. Zhou, F. R. Fan, W. Zhang, Z. Y. Zhou, D. Y. Wu, B. Ren, Z. L. Wang and Z. Q. Tian, *Nature*, 2010, **464**, 392–395.
- 5 R. A. Alvarez-Puebla and L. M. Liz-Marzán, *Chem. Soc. Rev.*, 2012, **41**, 43–51.
- 6 R. A. Alvarez-Puebla, A. Agarwal, P. Manna, B. P. Khanal, P. Aldeanueva-Potel, E. Carbó-Argibay, N. Pazos-Pérez, L. Vigderman, E. R. Zubarev, N. A. Kotov and L. M. Liz-Marzán, *Proc. Natl. Acad. Sci. U. S. A.*, 2011, **108**, 8157–8161.
- 7 F. Jäckel, A. A. Kinkhabwala and W. E. Moerner, *Chem. Phys. Lett.*, 2007, **446**, 339–343.
- 8 P. G. Etchegoin and E. C. Le Ru, *Phys. Chem. Chem. Phys.*, 2008, **10**, 6079–6089.
- 9 X. Su, J. Zhang, L. Sun, T. W. Koo, S. Chan, N. Sundararajan, M. Yamakawa and A. A. Berlin, *Nano Lett.*, 2005, **5**, 49–54.
- 10 C. M. Shachaf, S. V. Elchuri, A. L. Koh, J. Zhu, L. N. Nguyen, D. J. Mitchell, J. W. Zhang, K. B. Swartz, L. Sun, S. Chan, R. Sinclair and G. P. Nolan, *PLoS One*, 2009, **4**, e5206.
- 11 X. M. Qian, X. H. Peng, D. O. Ansari, Q. Yin-Goen, G. Z. Chen, D. M. Shin, L. Yang, A. N. Young, M. D. Wang and S. M. Nie, *Nat. Biotechnol.*, 2008, **26**, 83–90.
- 12 C. L. Zavaleta, B. R. Smith, I. Walton, W. Doering, G. Davis, B. Shojaei, M. J. Natan and S. S. Gambhir, *Proc. Natl. Acad. Sci. U. S. A.*, 2009, **106**, 13511–13516.
- 13 T. F. Massoud and S. S. Gambhir, *Genes Dev.*, 2003, **17**, 545–580.
- 14 A. G. Ryder, *Curr. Opin. Chem. Biol.*, 2005, **9**, 489–493.
- 15 Y. Zhang, H. Hong, D. V. Myklejord and W. Cai, *Small*, 2011, **7**, 3261–3269.
- 16 N. P. W. Pieczonka and R. F. Aroca, *Chem. Soc. Rev.*, 2008, **37**, 946–954.
- 17 K. L. Wustholz, A.-I. Henry, J. M. McMahon, R. G. Freeman, N. Valley, M. E. Piotti, M. J. Natan, G. C. Schatz and R. P. V. Duyne, *J. Am. Chem. Soc.*, 2010, **132**, 10903–10910.
- 18 L. Rodríguez-Lorenzo, R. n. A. Alvarez-Puebla, I. Pastoriza-Santos, S. Mazzucco, O. Stéphan, M. Kociak, L. M. Liz-Marzán and F. J. García de Abajo, *J. Am. Chem. Soc.*, 2009, **131**, 4616–4618.
- 19 C. G. Khoury and T. Vo-Dinh, *J. Phys. Chem. C*, 2008, **112**, 18849–18859.
- 20 V. Giannini, R. Rodríguez-Oliveros and J. Sánchez-Gil, *Plasmonics*, 2010, **5**, 99–104.
- 21 F. Hao, C. L. Nehl, J. H. Hafner and P. Nordlander, *Nano Lett.*, 2007, **7**, 729–732.
- 22 E. Budevski, E. Staikov and W. J. Lorenz, *Electrochemical Phase Formation and Growth*, VCH, Weinheim, 1996.
- 23 M. Paunovic and M. Schlesinger, *Fundamentals of Electrochemical Deposition*, Wiley, New Jersey, 2006.
- 24 G. S. Attard, P. N. Bartlett, N. R. B. Coleman, J. M. Elliott, J. R. Owen and J. H. Wang, *Science*, 1997, **278**, 838–840.
- 25 G. S. Attard, C. G. Goltner, J. M. Corker, S. Henke and R. H. Templer, *Angew. Chem., Int. Ed.*, 1997, **36**, 1315–1317.
- 26 K. M. Kulinkowski, P. Jiang, H. Vaswani and V. L. Colvin, *Adv. Mater.*, 2000, **12**, 833–838.
- 27 O. D. Velev, P. M. Tessier, A. M. Lenhoff and E. W. Kaler, *Nature*, 1999, **401**, 548.

- 28 J. Erlebacher, M. J. Aziz, A. Karma, N. Dimitrov and K. Sieradzki, *Nature*, 2001, **410**, 450–453.
- 29 S. Tominaka, Y. Nakamura and T. Osaka, *J. Power Sources*, 2010, **195**, 1054–1058.
- 30 S. Tominaka, T. Hayashi, Y. Nakamura and T. Osaka, *J. Mater. Chem.*, 2010, **20**, 7175–7182.
- 31 O. Okman and J. W. Kysar, *J. Alloys Compd.*, 2011, **509**, 6374–6381.
- 32 R. Morrish, K. Dorame and A. J. Muscat, *Scr. Mater.*, 2011, **64**, 856–859.
- 33 J.-S. Wi, E. S. Barnard, R. J. Wilson, M. L. Zhang, M. Tang, M. L. Brongersma and S. X. Wang, *ACS Nano*, 2011, **5**, 6449–6457.
- 34 Y. Lu and A. Penzkofer, *Chem. Phys.*, 1986, **107**, 175–184.
- 35 J. F. Moulder, W. F. Stickle, P. E. Sobol and K. D. Bomben, *Handbook of X-ray Photoelectron Spectroscopy*, Physical Electronics, Inc., Minnesota, USA, 1992.
- 36 S. Tominaka, *J. Mater. Chem.*, 2011, **21**, 9725–9730.
- 37 G. H. Chan, J. Zhao, E. M. Hicks, G. C. Schatz and R. P. Van Duyne, *Nano Lett.*, 2007, **7**, 1947–1952.
- 38 X. Y. Lang, L. Y. Chen, P. F. Guan, T. Fujita and M. W. Chen, *Appl. Phys. Lett.*, 2009, **94**, 213109.
- 39 L. Zhang, X. Lang, A. Hirata and M. Chen, *ACS Nano*, 2011, **5**, 4407–4413.
- 40 P. Hildebrandt and M. Stockburger, *J. Phys. Chem.*, 1984, **88**, 5935–5944.
- 41 A. Weiss and G. Haran, *J. Phys. Chem. B*, 2001, **105**, 12348–12354.
- 42 K. Kneipp, Y. Wang, R. R. Dasari and M. S. Feld, *Appl. Spectrosc.*, 1995, **49**, 780–784.
- 43 Y. Lu, G. L. Liu, J. Kim, Y. X. Mejia and L. P. Lee, *Nano Lett.*, 2005, **5**, 119–124.
- 44 K. Kneipp, Y. Wang, H. Kneipp, L. T. Perelman, I. Itzkan, R. Dasari and M. S. Feld, *Phys. Rev. Lett.*, 1997, **78**, 1667–1670.
- 45 F. J. GarciaVidal and J. B. Pendry, *Phys. Rev. Lett.*, 1996, **77**, 1163–1166.
- 46 J.-S. Wi, S. Sengupta, R. J. Wilson, M. Zhang, M. Tang and S. X. Wang, *Small*, 2011, **7**, 3276–3280.
- 47 W. Hu, M. L. Zhang, R. J. Wilson, A. L. Koh, J.-S. Wi, M. Tang, R. Sinclair and S. X. Wang, *Nanotechnology*, 2011, **22**, 185302.